Unwrapping differential x-ray phase-contrast images through phase estimation from multiple energy data

F. M. Epple,[1,*] G. Potdevin,[1] P. Thibault,[1] S. Ehn,[1] J. Herzen,[2] A. Hipp,[2] F. Beckmann[2] and F. Pfeiffer[1]

[1]*Physics Department, Technische Universitaet Muenchen,*
85748 Garching bei Muenchen, Germany
[2]*Institute of Materials Science, Helmholtz-Zentrum Geesthacht,*
21502 Geesthacht, Germany

[*]Franz.Epple@ph.tum.de

Abstract: We present a spectral phase unwrapping approach for grating-based differential phase-contrast data where the unwrapped interferometer phase shift is estimated from energy discriminated measurements using maximum likelihood principles. We demonstrate the method on tomographic data sets of a test specimen taken at different x-ray energies using synchrotron radiation. The proposed unwrapping technique was demonstrated to successfully correct the data set for phase wrapping.

OCIS codes: (100.5088) Phase unwrapping; (340.7450) X-ray interferometry; (110.4234) Multispectral and hyperspectral imaging.

References and links

1. A. Baldi, "Phase unwrapping by region growing," Appl. Opt. **42,** 2498–2505 (2003).
2. C. W. Chen and H. A. Zebker, "Two-dimensional phase unwrapping with use of statistical models for cost functions in nonlinear optimizatio," J.Opt. Soc. Am. A **18,** 338–351 (2001).
3. G. Nico, "Bayesian approaches to phase unwrapping: theoretical study," IEEE Trans. Sig. Process. **48,** 2454–2556 (2000).
4. D. Ghiglia and M. Pritt, *Two-Dimensional Phase Unwrapping: Theory, Algorithms, and Software* (Academic, 1998).
5. J. Kenntner, V. Altapova, T. Grund, F. J. Pantenburg, J. Meiser, T. Baumbach and J. Mohr, "Fabrication and characterization of analyzer gratings with high aspect ratios for phase contrast imaging using a Talbot interferometer," AIP Conference Proceedings. **1437**, 89–93 (2012).
6. C. David, J. Bruder, T. Rohbeck, C. Grnzweig, C. Kottler, A. Diaz, O. Bunk, F. Pfeiffer, "Fabrication of diffraction gratings for hard X-ray phase contrast imaging," Microelectron. Eng. **84**, 1172–1177 (2007).
7. I. Zanette, T. Weitkamp, S. Lang, M. Langer, J. Mohr, C. David, J. Baruchel, "Quantitative phase and absorption tomography with an X-ray interferometer and synchrotron radiation," Phys. Status Solidi **208**, 2526–2532 (2011).
8. K. Li, N. B. Bevins, J. N. Zambelli and G. Chen, "Feasibility of differential phase contrast CT for whole body imaging," AIP Conference Proceedings. **1466**, 175–180 (2012).
9. I. Jerjen, V. Revol, P. Schuetz, C. Kottler, R. Kaufmann, T. Luethi, K. Jefimovs, C. Urban and U. Sennhauser, "Reduction of phase artifacts in differential phase contrast computed tomography," Opt. Express **19**, 13604–13611 (2011).
10. W. Haas, M. Bech, P. Bartl, F. Bayer, A. Ritter, T. Weber, G. Pelzer, M. Willner, K. Achterhold, J. Durst, T. Michel, M. Prmmer, F. Pfeiffer, G. Anton, J. Hornegger, "Phase-Unwrapping of Differential Phase-Contrast Data using Attenuation Information," Proc. SPIE **7962**, (2011).
11. W. Xu, E. Chang, L. Kwoh, H. Lim, W. Cheng, A. Heng, "Phase-unwrapping of SAR Interferogram with Multi-frequency or Multi-baseline," in *Proceedings of IEEE Conference on Geoscience and Remote Sensing Symposium*, (*IEEE* 1994), pp. 730–732.

12. V. Pascazio and G. Schirinzi, "Multifrequency InSAR Height Reconstruction Through Maximum Likelihood Estimation of Local Planes Parameters," IEEE transaction on image processing, **11,** (2002).
13. J. Bioucas-Dias, V. Katkovnik, J. Astola, K. Egiazarian, *Multi-frequency Phase Unwrapping from Noisy Data: Adaptive Local Maximum Likelihood Approach*, (Academic, 2009), pp. 310–320.
14. D. Pennicard, S. Lange, S. Smoljanin, H. Hirsemann and H. Graafsma, "LAMBDA - Large Area Medipix3-Based Detector Array," JINST **7,** C11009 (2012).
15. R. Ballabriga, M. Campbell, E. Heijne, X. Llopart, L. Tlustos, W. Wong, "Medipix3: A 64k pixel detector readout chip working in single photon counting mode with improved spectrometric performance," Nucl. Instrum. Meth. A **633**, 15–18 (2011).
16. Medipix web site, www.cern.ch/medipix
17. R. Steadman, C. Herrmann, O. Mlhens, D. G. Maeding, J. Colley, T. Firlit, R. Luhta, M. Chappo, B. Harwood, D. Kosty, "ChromAIX: A high-rate energy-resolving photon-counting ASIC for Spectral Computed Tomography," Proc. of SPIE **7622**, 762220-1 – 762220-8 (2010).
18. C. Herrmann, R. Steadman, O. Mulhens, "ChromAIX: Fast energy resolved photon-counting readout electronics for Future Human Computed Tomography," in *Proceedings of IEEE Conference on Nuclear Science Symposium* (*IEEE*, 2010), pp. 1996-1999.
19. W. C. Barber, E. Nygard, J. C. Wessel, N. Malakhov, N. E. Hartsough, T. Gandhi, G. Wawrzyniak, J. S. Iwanczyk, "Photon-counting energy-resolving CdTe detectors for high-flux X-ray imaging," in *Proceedings of IEEE Conference on Nuclear Science Symposium* (*IEEE*, 2010), 3953–3955.
20. A. Momose, S. Kawamoto, I. Koyama, Y. Hamaishi, K. Takai and Y. Suzuki, "Demonstration of X-ray Talbot Interferometry," Jpn. J. Appl. Phys., **42,** 866–868 (2003).
21. A. Momose, W. Yashiro, Y. Takeda, Y. Suzuki, T. Hattori, "Phase tomography by X-ray Talbot interferometry for biological imaging," Jpn. J. Appl. Phys. **45**, (2006).
22. T. Weitkamp, A. Diaz, C. David, F. Pfeiffer, M. Stampanoni, P. Cloetens, E. Ziegler "X-ray phase imaging with a grating interferometer, " Opt. Express **13**, 6296–6304 (2005).
23. F. Pfeiffer, T. Weitkamp, O. Bunk and C. David, "Phase retrieval and differential phase-contrast imaging with low-brilliance X-ray sources," Nature Phys. Lett. **2,** 258–261 (2006).
24. D. Attwood, *Soft X-rays and Extreme Ultraviolet Radiation* (Academic, 2005).
25. F. Pfeiffer, M. Bech, O. Bunk, P. Kraft, E. F. Eikenberry, C. Brnnimann, C. Grnzweig, C. David, "Hard-X-ray dark-field imaging using a grating interferometer," Nature Mater. **7,** 134–137 (2008).
26. F. Pfeiffer, M. Bech, O. Bunk, T. Donath, B. Henrich, P. Kraft, C. David, "X-ray dark-field and phase-contrast imaging using a grating interferometer," J. Appl. Phys. **105**, 102006 (2009).
27. M. Born and E. Wolf, *Principles of Optics* (Academic, 1993).
28. M. Engelhardt, J. Baumann, M. Schuster, C. Kottler, F. Pfeiffer, O. Bunk, C. David, "High-resolution differential phase contrast imaging using a magnifying projection geometry with a microfocus X-ray source," Appl. Phys. Lett. **90**, 224101 (2007).
29. A. N. Tikhonov, "On the stability of inverse problems," Doklady Akademii Nauk SSSR **39,** 195–198 (1943).
30. J. Herzen, T. Donath, F. Beckmann, M. Ogurreck, C. David, J. Mohr, F. Pfeiffer, A. Schreyer, "X-ray grating interferometer for materials-science imaging at a low-coherent wiggler source," Rev. Sci. Instrum. **82,** (2011).
31. The Phantom Laboratory, *Catphan 504 Manual* (2012).

1. Introduction

For a wide range of imaging techniques, such as magnetic resonance imaging (MRI), synthetic aperture radar (SAR) or phase-contrast imaging (PCI) the phase of a measured periodic signal is the quantity of interest. However, the intrinsic periodic nature of the phase quantity leads to signal wrapping when measuring and converting the physical quantity of interest, if the original signal exceeds 2π. Correcting for this effect is known as phase unwrapping, and is a very active research area in digital imaging. Depending on the situation, unwrapping can become challenging, for example, because of noise. Various unwrapping solutions have been proposed for a wide range of applications, such as region growing algorithms, statistical models and Bayesian approaches among others [1–4].

In grating-based differential phase imaging (gbDPI) phase wrapping occurs when the beam deflection, due to a strong refraction by the sample, exceeds the ratio of the analyzer grating period to its distance from the point of deflection [5, 6]. Hence, to reduce or avoid phase wrapping, either the refraction angle or the sensitivity of the interferometer needs to be reduced. But in many cases a high sensitivity of the interferometer is needed to resolve small signal differences, e.g. in biological soft-tissues, and phase wrapping occurs at higher deflecting regions
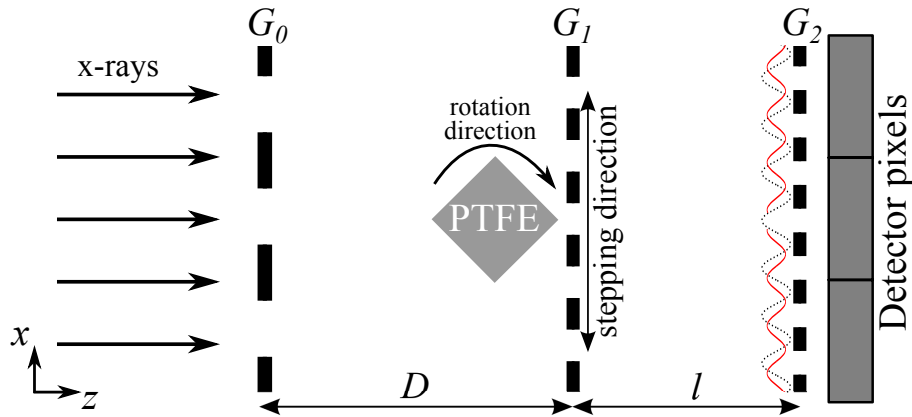
Fig. 1. Sketch of the Talbot-Lau interferometer. It consists of the source grating G_0 with period p_0, the phase grating G_1 with period p_1 and the analyzer grating G_2 with period p_2. In this case, the G_1 grating was used for the stepping process. The doted black curve and the continuous red curve illustrate the interference pattern without and with a sample in the x-ray beam, respectively.

of the sample. For example the presence of bone or air cavities in soft tissue leads to strong phase wrapping which strongly corrupts the 3-D tomographic reconstruction [7, 8]. Existing approaches to correct or reduce phase wrapping errors in differential phase data make use of the attenuation contrast, which is simultaneously obtained [9, 10]. Those approaches are very promising, for example in non-destructive testing, but as they rely on a good attenuation contrast, they might fail in biomedical imaging where the attenuation contrast is weak.

Here we show that, for gbDPI, the phase unwrapping problem can be solved efficiently, exploiting the energy dependency $(1/E^2)$ of the phase shift using measurements at different energies followed by a maximum likelihood estimation [11–13]. The spectral x-ray image data can be either obtained with specially designed x-ray imaging detectors, which are currently in use or under development [14–19], or by using tunable monochromatic x-ray sources. In this study we used the latter alternative, and performed the experiments using multiple selected and highly monochromatic $(\Delta E/E \sim 10^{-1})$ x-rays from a synchrotron source.

2. Principles

The spatial derivative of the phase shift Φ, which an x-ray wavefront experiences when it passes through an object, can be measured using an x-ray interferometer [20–22]. In Fig. 1 the three grating Talbot-Lau interferometer is illustrated, which uses the first attenuation grating G_0 with period p_0 to match the spatial coherence of the low brilliance x-ray source [23]. The phase grating G_1 placed at a distance D with period p_1 produces an interference pattern with a period p_2 further downstream. When a sample is introduced into the beam path, the interference pattern is shifted, due to refraction caused by the varying phase [24]. Measuring this interference pattern phase shift φ allows to extract the spatial derivative of the phase shift introduced by the sample (i.e. $\frac{\partial \Phi}{\partial x}$). However, the period of the interference pattern and its phase shift is typically too small to be directly spatially resolved with a common x-ray detector. For this reason the second attenuation grating G_2, which has the same period p_2 as the interference pattern, is placed at a distance l from G_1. The interference pattern is then sampled by stepping one of the gratings (in our case G_1) laterally in x-direction while the intensity I is measured at each grating position x_g. As a result, the intensity I as a function of x_g contains the information about the interference

pattern phase shift φ as well as the absorption signal $\langle I \rangle$ which contains the information about the absorption of the x-rays and the signal A_1 which contains the information about the small angle scattering of the x-rays within the specimen. Assuming a sinosoidal variation of the signal, those parameters can finally be obtained from the first components f_0 and f_1 of the Fourier transform of I [25]:

$$f_0 = \frac{1}{N} \sum_{s=0}^{N-1} I_s = \langle I \rangle, \tag{1a}$$

$$f_1 = \frac{1}{N} \sum_{s=0}^{N-1} I_s e^{-\frac{2\pi i}{N} s} = \frac{1}{2} A_1 e^{i\varphi}. \tag{1b}$$

Here N is the total number of regularly spaced stepping points (i.e. total number of x_g positions) and I_s is the measured intensity in the relevant pixel at step s. From $\langle I \rangle$ and A_1 we can obtain the conventional attenuation contrast and respectively the so called dark-field contrast which arises from the small angle scattering. The interference pattern phase shift φ, relative to an undisturbed interference pattern without the object in the beam, is proportional to the spatial derivative of the object phase shift Φ introduced by the sample [27, 28]:

$$\varphi(x,y) = \frac{l\lambda}{p_2} \frac{\partial \Phi}{\partial x} \tag{2a}$$

$$= \frac{l}{p_2} r_e \lambda^2 \frac{\partial}{\partial x} \int_{Sample} \rho(x,y,z)\,\mathrm{d}z \tag{2b}$$

$$= \lambda^2 M. \tag{2c}$$

Here l denotes the distance between the analyzer grating G_2 and the phase grating G_1, λ is the x-ray wavelength, r_e the classical electron radius and ρ the electron density of the sample. In Eq. (2c) we combined the energy-independent parameters into $M = \frac{l}{p_2} r_e \frac{\partial}{\partial x} \int \rho(x,y,z)\,\mathrm{d}z$. In the current context, phase wrapping occurs when the interference pattern phase shift φ exceeds its scope of 0 to 2π leading to an observed phase shift of

$$\varphi = \Psi \text{ modulo } 2\pi, \tag{3}$$

where Ψ is the unwrapped interference pattern phase shift we are looking for.

In an imaging experiment, we are only interested in the unknown sample parameters which we included into the energy-independent term M, and more specifically the electron density of the material therein, of Eq. (2c). Consequently, the invariance of M with respect to the x-ray energy allows to obtain multiple values of M when φ is measured at different x-ray energies. Hence, if k different energy bins E_j with $j = 1,...,k$ are used we obtain k values for M which we can assume to be Gaussian distributed due to the different counting statistic, which is a consequence of the x-ray source statistic. Because the measurements are statistically independent, we evaluate the maximum likelihood estimator (ML) for M by minimizing the following likelihood function L

$$L(\varphi_j, M) \propto \prod_j \exp\left(-\frac{1}{(2\sigma_j^2)} \left| f_{1j} - \frac{1}{2} A_{1j} e^{i\lambda_j^2 M} \right|^2\right) \tag{4a}$$

$$\propto \prod_j \exp\left(-\frac{A_{1j}^2}{8\langle I \rangle_j} \left| e^{i\varphi_j} - e^{i\lambda_j^2 M} \right|^2\right), \tag{4b}$$
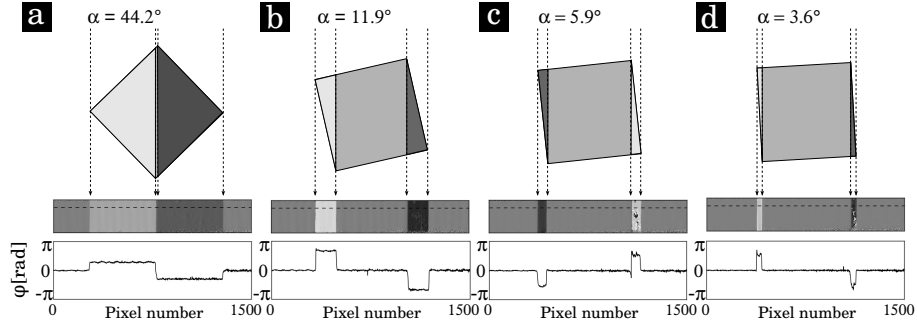
Fig. 2. The top row shows a sketch of the plastic (*PTFE*) cube test specimen at rotation angle α. The x-ray propagation direction is illustrated by the dashed arrows. The middle and bottom rows show the measured projections of the interference pattern phase shift φ and the corresponding line plots along the dashed lines, respectively. The projections where taken at an x-ray energy of 24 keV. Since phase wrapping is present in c) and d), the measured interference pattern phase shift is not anymore proportional to the actual differential phase shift of the object as expressed by Eq. (3).

where we have assumed the counting statistics to be the main source of noise. This assumption holds for all photon counting detectors, so that $\sigma_j^2 = \langle I \rangle_j$. From (4b) we obtain the estimated M by minimizing the following negative log-likelihood function ℓ

$$\ell = -\log(L) \propto \sum_j \frac{A_{1_j}^2}{\langle I \rangle_j} \left(1 - \cos(\varphi_j - \lambda_j^2 M) \right) + \beta R^2. \tag{5}$$

Experimental conditions are always such that smaller values of M are more probable. This assumption is enforced by the Tikhonov regularization βR^2 with a suitable factor β [29].

The evaluation of the ML estimator from measurements at different energies brings several advantages:

First, the ML estimator can still be retrieved correctly even if φ wraps in each individual measurement. Second, we effectively increase the signal-to-noise ratio, incorporating an explicit gbDPI noise model into the ML estimator. Further, relying on more than one measurement makes this approach robust against low counting statistics and the capability is only limited to the effective signal-to-noise ratio of all measurements. Finally, in contrast to most existing 2-D phase unwrapping techniques our method does not rely on the information of neighbouring pixels. Instead, each pixel is processed individually and errors possibly arising during the unwrapping process, even though they are quite unlikely with state of the art unwrapping algorithms, do not propagate through the image. In general, the reliability of this approach and its robustness against noise improves with the number of distinct energies, which ideally should cover a wide range of the x-ray source spectrum.

3. Experimental results

To test our method experimentally, we performed tomographic measurements of a plastic (*PTFE*) cube test sample at different x-ray energies at the beamline HARWI II, operated by the Helmholtz-Zentrum Geesthacht, at the synchrotron DESY in Hamburg. Because of its flat edges, a cube object is difficult to reconstruct from differential phase-contrast projections since strong phase wrapping occurs when the angle between its facets and the incoming x-rays becomes small. To measure the interference pattern phase shift we used the Talbot-Lau interferometer installed at the beamline [30]. The inter-grating distances were $D = 3.0$ m between the
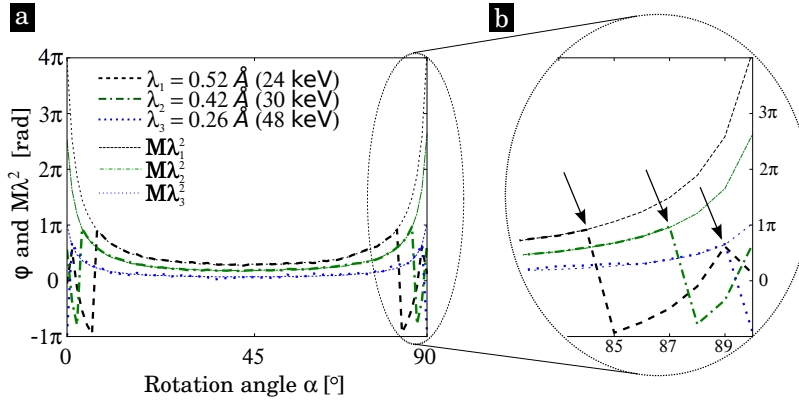
Fig. 3. a) The interference pattern phase shifts φ for $\lambda_1 = 0.52\,\text{Å}$ (thick black), $\lambda_2 = 0.42\,\text{Å}$ (thick green) and $\lambda_3 = 0.26\,\text{Å}$ (thick blue) together with the estimated interference pattern phase shift $M\lambda^2$ (thin lines) for all x-ray wavelength from a single pixel over a $90°$ rotation of the cube. b) Zoom into the area where phase wrapping, indicated by arrows, occurs.

source and the phase grating and $l = 0.32\,\text{m}$ between the phase and the analyzer grating. The periods of the gratings were $22.3\,\mu\text{m}$, $4.33\,\mu\text{m}$ and $2.4\,\mu\text{m}$ for the source, phase and analyzer grating, respectively.

The interferometer showed good performance (i.e. high visibility) at energies of $24\,\text{keV}$, $30\,\text{keV}$ and $48\,\text{keV}$ which were therefore chosen for the measurements. For each tomography scan we took 301 projections, equally spaced over $360°$, while each projection was taken with 4 phase steps and an exposure time of $2\,\text{s}$ per step. To record the images a $580\,\mu\text{m}$ thick $CdWO_4$ scintillator lens-coupled to a CCD camera with an effective pixel size of $10\,\mu\text{m}$ was used.

Figure 2 (second and third row) depicts the interference pattern phase shift φ of the cube at an x-ray energy of $24\,\text{keV}$ for different rotation angles α. From a cube, only the regions indicated with white and black triangles lead to a positive and negative interference pattern phase shift respectively. In the gray region the phase shift Φ induced by the object is constant and no interference pattern phase shift occurs as it derives from Eq. (2a). Due to the increasing gradient of the facets the interference pattern phase shift φ increases as the cube is rotated. Phase wrapping could be observed at rotation angles smaller than $\alpha < 8°$ as shown in Fig. 2(c) and Fig. 2(d). At those angles the measured interference pattern phase shift is not anymore proportional to the actual differential phase shift of the object as expressed by Eq. (3).

The attempt of a tomographic reconstruction with filtered back projection of a data set containing such phase wraps is corrupted by strong streak artifacts. To correct for those artifacts we used all measured interference pattern phase shifts at $24\,\text{keV}$, $30\,\text{keV}$ and $48\,\text{keV}$ to estimate the unwrapped interference pattern phase shift $M\lambda^2$ by minimizing the cost function [Eq. (5)]. In order to find the global minimum, we evaluated Eq. (5) for a large number of discrete values of M, with constant spacing and selected the M which lead to a minimal ℓ. The precision in the evaluation of M is therefore dependent on the chosen spacing, and the processing time on the total number of values of M which are evaluated. There is no doubt that more advanced algorithms can be used to improve accuracy and to reduce processing time. The regularization was defined as $R = \frac{M}{M_{max}}$ where M_{max} is the maximum value of M which we tested to find the global minimum and a Tikhonov factor $\beta = 4$ was used.

The result for a single pixel is depicted in Fig. 3, where the measured interference pattern phase shift φ for all x-ray energies as well as the corresponding estimated values $M\lambda^2$ for a rotation of the cube from $0°$ to $90°$ is shown. The angles where phase wrapping occurs are
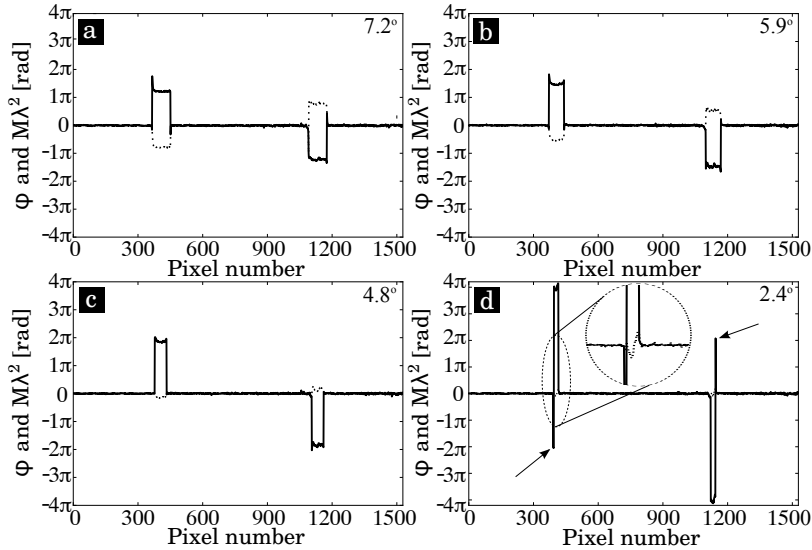
Fig. 4. Measured (dashed) and estimated (solid) interference pattern phase shift φ and $M\lambda^2$ respectively at an x-ray energy of 24 keV for 4 different rotation angles of the cube. The arrows in d) indicate the artifacts which derive from the total external reflection of the x-rays at the surface of the cube.

indicated by arrows. The strength of the interference pattern phase shift φ depends further on the x-ray energy as given in Eq. (2). Since φ decreases with increasing energy phase wrapping tends to occur at smaller angles for higher energies. At an rotation angle of 1.6° the signal has wrapped at even the highest energy, but a correct estimation of M was still obtained.

Figure 4 shows the profile of the measured interference pattern phase shift φ together with the estimated interference pattern phase shift $M\lambda^2$ at 4 different rotation angles for an x-ray energy of 24 keV. As can be seen, the method is able to estimate the interference pattern phase shift also at angles where the deflection angle exceeds multiple times the direct detectable value of p_2/l. A comparison of the reconstructed electron densities from the measured and estimated interference pattern phase shifts in Fig. 5(a) and Fig. 5(b) demonstrates the quantitative improvement. Within the region marked with the dashed square we extracted mean electron densities of $\rho_m = (4.79 \pm 0.93) \times 10^{29} m^{-3}$ and $\rho_e = (5.59 \pm 0.61) \times 10^{29} m^{-3}$ from the measured and estimated reconstruction respectively. Compared to the value in literature $\rho_{lit} = 6.24 \times 10^{29} m^{-3}$ the error could be reduced by a factor of 2.23 [31]. The line plot through the uncorrected slice (continuous curve in Fig. 5(c)) shows that the square profile of the cube is strongly blurred, due to the phase wrapping artifacts. On the other hand, the line plot through the corrected slice (dashed curve in Fig. 5(c)) exhibits nearly the expected square profile of the cube. The derivation from a perfect square profile and the reason for the too low electron density are mainly caused by the remaining streak artifacts which have their origin in distinct effects. First, this unwrapping approach comes to its limits at points where the phase gradient shows singularities. In addition, total external reflection of the x-rays occurred at small glancing angles. This effect can also be seen in Fig. 4(d) where the sharp spikes (indicated by arrows) are a result of those reflections which cause streak artifacts in the 3D reconstruction.
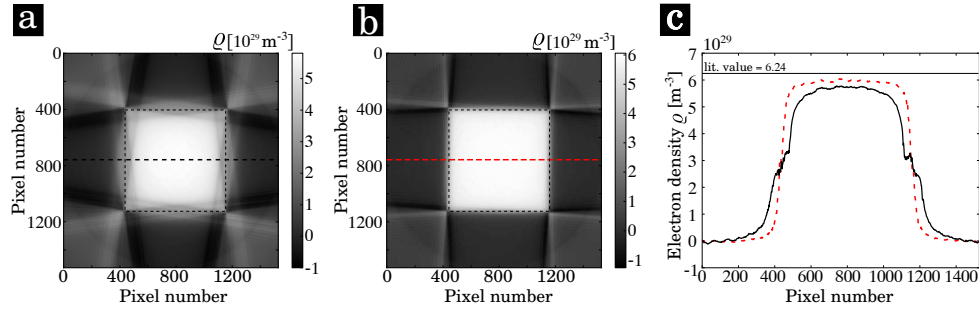
Fig. 5. Slices through the reconstructed electron density from a) the measured interference pattern phase shift at 24 keV and b) from the estimated energy independent interference pattern phase shift M. The dashed squares indicate the area from which we extracted the mean electron densities of $\rho_m = (4.79 \pm 0.93) \times 10^{29} m^{-3}$ and $\rho_e = (5.59 \pm 0.61) \times 10^{29} m^{-3}$ from the measured and estimated interference pattern phase shift, respectively. c) Line plots along the horizontal lines of a) (continuous) and b) (dashed).

4.   Discussion and conclusion

In conclusion we could demonstrate a method to estimate the unwrapped interference pattern phase shift φ from a set of gbDPI measurements performed at various energies. For that we proposed to evaluate the maximum likelihood estimator by minimizing a suitable likelihood function and were able to show its efficiency in a proof of principle experiment. In contrast to the presented experiment, the measurement of the interference pattern phase shift at different energies can simultaneously be performed using a polychromatic x-ray source in combination with an energy-sensitive detector. This is in particular of interest for experiments where the total radiation dose applied to the specimen might be an issue. The efficiency of this method depends on the properties of the sample, such as the amount of attenuation, phase shift and scattering of the x-rays. Further, the x-ray source spectrum, the number and the range of selected energies, the changing interferometer performance at different energies, as well as the regularization will have an impact on its success. A detailed analysis of the mentioned influences and a quantitative evaluation of the final signal-to-noise ratio and thus, the relative improvement of the method with respect to existing methods will be subject of following studies. We believe that this study will be of particular interest to the biomedical imaging community, which pushes for the implementation of spectral x-ray imaging detection schemes right now, and the x-ray phase-contrast modality in the near future.

Acknowledgments